frontiers | Frontiers in Chemistry

TYPE Original Research
PUBLISHED 20 October 2023
DOI 10.3389/fchem.2023.1271556

OPEN ACCESS

EDITED BY
Gangbing Zhu,
Jiangsu University, China

REVIEWED BY
Preeti Gupta,
Leibniz Institute for Solid State and Materials Research Dresden (IFW Dresden), Germany
Nan Hao,
Jiangsu University, China

*CORRESPONDENCE
Yinquan Wang,
wyq19690120@163.com
Fei Yan,
yanfei@zstu.edu.cn

RECEIVED 02 August 2023
ACCEPTED 04 October 2023
PUBLISHED 20 October 2023

CITATION
Guo Q, Fan X, Yan F and Wang Y (2023), Highly sensitive electrochemical immunosensor based on electrodeposited platinum nanostructures confined in silica nanochannels for the detection of the carcinoembryonic antigen.
Front. Chem. 11:1271556.
doi: 10.3389/fchem.2023.1271556

Highly sensitive electrochemical immunosensor based on electrodeposited platinum nanostructures confined in silica nanochannels for the detection of the carcinoembryonic antigen

Qinping Guo[1], Xue Fan[2], Fei Yan[2]* and Yinquan Wang[1]*

[1]Shanxi Bethune Hospital, Shanxi Academy of Medical Sciences, Tongji Shanxi Hospital, Third Hospital of Shanxi Medical University, Taiyuan, China, [2]Key Laboratory of Surface and Interface Science of Polymer Materials of Zhejiang Province, Department of Chemistry, Zhejiang Sci-Tech University, Hangzhou, China

In this study, we report a highly sensitive electrochemical immunosensor for carcinoembryonic antigen (CEA) detection based on the electrodeposited platinum nanoparticles (Pt NPs) confined in the ultrasmall nanochannels of vertically ordered mesoporous silica film (VMSF). VMSF bearing amine groups (NH_2-VMSF) can be prepared on the indium tin oxide electrode surface via a one-step co-condensation route using an electrochemically assisted self-assembly method, which renders a strong electrostatic effect for $[PtCl_6]^{2-}$ and leads to the spatial confinement of Pt NPs inside the silica nanochannels after electrodeposition. The external surface of NH_2-VMSF is functionalized with CEA antibodies using glutaraldehyde as a coupling agent, resulting in an electrochemical immunosensing interface with good specificity for CEA detection. Under optimal experimental conditions, high affinity between the CEA antibody and CEA produces a steric hindrance effect for the accessibility of the electrochemical probe ($[Fe(CN)_6]^{3-}$) in the bulk solution to the underlying indium tin oxide surface, eventually resulting in the attenuated electrochemical signal and enabling the detection of the CEA with a wide linear range of 0.01 pg/mL~10 ng/mL and a pretty low limit of detection of 0.30 fg/mL. Owing to the signal amplification ability of Pt NPs and the anti-biofouling property of NH_2-VMSF, the as-prepared electrochemical immunosensor based on the Pt NPs@NH_2-VMSF displays an accurate analysis of the CEA in human serum samples, holding significant promise for health monitoring and clinical diagnosis.

KEYWORDS

platinum nanoparticles, silica nanochannel films, electrochemical immunosensor, carcinoembryonic antigen, anti-fouling detection

1 Introduction

Nanomaterials usually exhibit a large specific surface area and unique magnetic/optical/electrochemical properties that can improve the sensitivity and selectivity of various chemo/biosensors (Mao et al., 2019; Xi et al., 2019; Qiu et al., 2021; Zheng et al., 2021; Huang Y. et al., 2023; Xu et al., 2023; Zhu et al., 2023). Among them, noble metal nanoparticles (NPs) with nanosized structures have garnered significant attention due to their unique physicochemical

properties and large specific surface area compared to their bulk materials, which have been widely used in electroanalytical applications (Lin et al., 2020; Zhao et al., 2020). Platinum (Pt) NPs are a kind of commonly used noble metal NP but unstable and will aggregate because of their high surface energy, resulting in the disappearance of specific desired features at the ultrasmall nanoscale. To control Pt NPs at the nanoscale, organic ligands or particular supported materials are introduced in the preparation procedure (White et al., 2009).

Recently, nanoporous materials have gained significant attention due to their high specific surface area, adjustable structure, and pore size and have exhibited considerable potential in applications such as adsorption/separation, sensing, catalysis, and energy storage applications (Cui et al., 2020; 2021; Zhao et al., 2020; Gong et al., 2022a; Liu et al., 2022). Vertically ordered mesoporous silica films (VMSFs) are a kind of solid nanoporous materials composed of highly ordered and uniform silica nanochannels (2–3 nm in diameter and tens to a hundred nanometers in length) and high porosity (Walcarius, 2021; Huang J. et al., 2023; Deng et al., 2023). In the past decades, an increasing number of electrochemical and electrochemiluminescence sensors have been designed using VMSF as the electrode-modified material (Liang et al., 2021; Su et al., 2022; Wei et al., 2022; Zhou et al., 2022). Although VMSF has unique insulating properties, it has been extensively utilized as an electrode protective layer for the direct and highly sensitive anti-biofouling analysis of complicated media (Wang et al., 2022; Zheng et al., 2022; Zhu et al., 2022). On the one hand, VMSFs bearing a large amount of silanol groups (pK_a = 2–3) display pronounced permselective effects toward targets or probes and simultaneously have excellent molecular sieving capability for them (Luo et al., 2022; Lv et al., 2022). On the other hand, they offer a lot of tiny confined spaces for the synthesis of metal NPs (e.g., gold (Ding et al., 2014a; Huang L. et al., 2023), Pt (Ding and Su, 2015; Li et al., 2020), and nickel (Ding et al., 2020)), polymers (Ding et al., 2014b), and graphene quantum dots (Zhang C. et al., 2023). The Su group employed two methods (namely, direct electrodeposition and chemical reduction) to achieve Pt NPs in silica nanochannels (Ding and Su, 2015; Li et al., 2020). The latter one needs first confinement of polyaniline polymer inside the nanochannels, generating the secondary and tertiary imines for easy complex with $PtCl_6^{2-}$ and subsequently suffering from chemical reduction *in situ*. To the best of our knowledge, simple modification of VMSF with functional groups for adequate incorporation of $PtCl_6^{2-}$ and further electrodeposited growth of Pt NPs has not yet been reported. Moreover, VMSF with functional groups renders the binding site for immobilization of specific recognition elements, exhibiting promising ability for the development of various sensitive and selective electrochemical sensors (Gong et al., 2022b; Ma et al., 2022b; Zhang T. et al., 2023; Chen et al., 2023).

Screening of tumor markers in human serum, especially the level of the carcinoembryonic antigen (CEA), is particularly valuable for the early auxiliary diagnosis and prognosis of various cancers (Zhang et al., 2022; Zhou et al., 2023). CEA concentration in the blood serum of healthy individuals is generally below 5 ng/mL, whereas cancer patients may exhibit levels exceeding 20 ng/mL (Lin et al., 2021). Several strategies have been developed for CEA detection, such as the enzyme-linked immunosorbent assay (Song et al., 2017), electrochemiluminescence method (Zhang et al., 2017), immunohistochemical method (Zeng et al., 1993), radioimmunoassay (Edgington et al., 1976), fluoroimmunoassay (Huang et al., 2018), and electrochemical immunoassay (Tang et al., 2007; Yan et al., 2023). Among them, electrochemical immunoassay has many advantages because of its low cost, rapid response, high selectivity, easy operation, and portability. Therefore, the development of electrochemical sensors with high sensitivity and anti-fouling capacity for direct detection of the CEA in human serum is highly desirable.

In this work, we demonstrate the use of amino group-functionalized VMSF (NH_2-VMSF) for the confined synthesis of Pt NPs and the design of a highly sensitive electrochemical immunosensor for the CEA. NH_2-VMSF-carrying amino groups provide a strong electrostatic effect for $[PtCl_6]^{2-}$ and lead to the well confinement of Pt NPs after electrodeposition. Such obtained Pt NPs confined in ultrasmall nanochannels of NH_2-VMSF (termed as Pt NPs@NH_2-VMSF) can be obtained in several seconds using a simple and controllable electrochemical method. The external surface of NH_2-VMSF is immobilized with CEA antibodies using glutaraldehyde as a coupling agent, giving rise to an electrochemical immunosensing interface with good specificity for CEA detection. Due to the high affinity between the CEA antibody and CEA on the sensing interface, the steric hindrance effect is enhanced for the accessibility of the electrochemical probe ($[Fe(CN)_6]^{3-}$) in the bulk solution to the underlying ITO surface, ultimately yielding the relationship between the attenuated electrochemical signal and CEA concentration. Benefiting from the signal amplification ability of Pt NPs and the anti-biofouling property of NH_2-VMSF, the developed electrochemical immunosensor based on Pt NPs@NH_2-VMSF can be applied to sensitively and selectively detect CEA in human serum.

2 Materials and methods

2.1 Chemicals and materials

The CEA antigen and anti-CEA antibody, prostate-specific antigen (PSA), and alpha-fetoprotein (AFP) were purchased from Beijing Key-Bio Biotech Co., Ltd. (Beijing, China). S100 calcium-binding protein β was bought from Proteintech (Wuhan, China). C-reactive protein (CRP) was ordered from Nanjing Okay Biotechnology Co., Ltd. (Nanjing, China). Hexadecyl trimethyl ammonium bromide (CTAB), silicon tetraacetate (TEOS), potassium ferricyanide ($K_3[Fe(CN)_6]$, 99.5%), potassium ferrocyanide ($K_4[Fe(CN)_6]$, 99.5%), sodium dihydrogen phosphate dihydrate ($NaH_2PO_4{\cdot}2H_2O$), sodium phosphate dibasic dodecahydrate ($Na_2HPO_4{\cdot}12H_2O$), glutaraldehyde (GA), and chloroplatinic acid hexahydrate ($H_2PtCl_6{\cdot}6H_2O$) were received from Aladdin Biochemical Technology Co., Ltd. (Shanghai, China). 3-Aminopropyltriethoxysilane (APTES) and potassium hydrogen phthalate (KHP) were purchased from Shanghai Macklin Biochemical Co., Ltd. (Shanghai, China). Sodium nitrate ($NaNO_3$), sodium hydroxide (NaOH), and ethanol (99.8%) were purchased from Hangzhou Gaojing Fine Chemical Co., Ltd. (Hangzhou, China). Concentrated hydrochloric acid (HCl) and concentrated sulfuric acid (H_2SO_4) were obtained from Shuanglin Inorganic Chemical Plant

(Hangzhou, China). Phosphate buffer solution (PBS) was prepared by mixing Na_2HPO_4 and NaH_2PO_4.

ITO-coated glasses (<17 Ω/square, thickness: 100 ± 20 nm) were purchased from Zhuhai Kaivo Optoelectronic Technology Co., Ltd. (China). To get a clean surface, the ITO electrode was immersed in 1 M NaOH solution overnight and then successively sonicated in acetone, ethanol, and ultrapure water. Ultrapure water (18.2 MΩ cm) used in the experiments was prepared by using the Milli-Q system (Millipore Company).

2.2 Measurements and instrumentations

Transmission electron microscopy (TEM) images were captured using a transmission electron microscope (JEM-2100, JEOL, Japan). Field-emission scanning electron microscopy (SEM) images and energy dispersive X-ray mapping spectroscopy (EDS mapping) data were analyzed using a scanning electron microscope (Sigma500, Zeiss, Germany). The X-ray photoelectron spectroscopy (XPS) data were collected on a PHI5300 electron spectrometer using 250 W, 14 kV, and Mg Kα radiation (PE Ltd., United States). All electrochemical measurements, including cyclic voltammetry (CV), electrochemical impedance spectroscopy (EIS), and differential pulse voltammetry (DPV), were conducted on a conventional three-compartment electrochemical cell by Autolab (PGSTAT302N) electrochemical workstation (Metrohm, Switzerland), with the modified ITO electrode, an Ag/AgCl electrode, and a platinum wire electrode as the working, reference, and counter electrodes, respectively. The scan rate for CV tests was 50 mV/s. The parameters for DPV measurements included step potential (0.005 V), pulse amplitude (0.05 V), pulse time (0.05 s), and interval time (0.2 s).

2.3 Preparation of SM@NH_2-VMSF/ITO and GA/Pt NPs@NH_2-VMSF/ITO electrodes

The NH_2-VMSF/ITO could be grown on the bare ITO electrode (1 cm × 0.5 cm) by the electrochemically assisted self-assembly (EASA) method within 10 s (Etienne et al., 2009; Ma et al., 2022a; Ma N. et al., 2022). In brief, CTAB (1.585 g) was first dissolved in a mixture solution consisting of 0.1 M $NaNO_3$ aqueous solution (20 mL, pH 2.6) and ethanol (20 mL). After the addition of APTES (0.318 mL), the pH of the mixed solution was adjusted to 2.97 using 6 M HCl. Subsequently, TEOS (2.372 mL) was added, and the obtained precursor solution was stirred at room temperature for 2.5 h. VMSF-bearing amino groups (NH_2-VMSF) were prepared on the bare ITO electrode surface by immersing the clean ITO electrode in the aforementioned aged solution and applying a constant current density (−0.70 mA·cm^{-2}) for 10 s. Then, the finally obtained electrode was rapidly washed with ultrapure water and aged for 12 h at 120°C. As for the directly as-prepared modified electrode, surfactant micelles (SMs) made up of CTAB were positioned inside the nanospace of silica nanochannels, designated as SM@NH_2-VMSF/ITO.

GA-functionalized SM@NH_2-VMSF/ITO, termed GA/SM@NH_2-VMSF/ITO, was obtained using a simple drop-casting procedure, which could act as a cross-linking agent for further covalent immobilization of specifically recognized antibodies. Specifically, 5% GA (50 μL) was dropped onto the SM@NH_2-VMSF/ITO electrode surface and incubated at 37°C for 30 min in a dark place. Then, the GA/SM@NH_2-VMSF/ITO electrode was placed into a 0.1 M HCl/ethanol solution under stirring for 5 min to remove the SM, generating open channels for mass transport. Such resulting electrode was denoted as GA/NH_2-VMSF/ITO. Pt nanoparticles were electrodeposited inside NH_2-VMSF using chronoamperometry, and the growth of Pt NPs can be well controlled when applying a constant potential of −0.2 V for different durations. 3.86 mM of $H_2PtCl_6{\cdot}6H_2O$ electrodeposition solution was composed of 100 mg/mL $H_2PtCl_6{\cdot}6H_2O$ (1 mL) and 0.1 M H_2SO_4 (49 mL). In short, the GA/NH_2-VMSF/ITO electrode was immersed in the aforementioned electrodeposition solution and applied a constant potential of −0.2 V for 2 s, finally achieving the Pt NPs confined into the nanochannels of NH_2-VMSF, designated as GA/Pt NPs@NH_2-VMSF/ITO.

2.4 Preparation of the electrochemical immunosensor based on the GA/Pt NPs@NH_2-VMSF/ITO electrode and electrochemical determination of CEA

An electrochemical immunosensor for CEA detection was prepared by immersing the GA/Pt NPs@NH_2-VMSF/ITO electrode in a 10 μg/mL antibody-CEA (50 μL) solution and incubating at 4°C for 1 h. After being rinsed with the residual antibody-CEA with 0.01 M PBS (pH 7.4), the immunosensing interface was eventually obtained, named the Ab/GA/Pt NPs@NH_2-VMSF/ITO electrode.

CEA solution (50 μL) with various concentrations was dropped onto the Ab/GA/Pt NPs@NH_2-VMSF/ITO electrochemical immunosensor and incubated at 4°C for 1 h. Then, the residual CEA solution was washed off using 0.01 M PBS (pH 7.4). DPV was utilized to measure the electrochemical signal of $[Fe(CN)_6]^{3-}$ before and after the interaction between Ab/GA/Pt NPs@NH_2-VMSF/ITO and CEA. Moreover, the standard addition method was used for the determination of CEA in fetal bovine serum to prove the reliability of the constructed Ab/GA/Pt NPs@NH_2-VMSF/ITO immunosensor in real samples. The fetal bovine serum was diluted by a factor of 50 using 0.01 M PBS (pH 7.4), and the CEA with a known concentration was added to the serum sample. Finally, the same detection procedure was conducted on the CEA detection in the serum sample using the Ab/GA/Pt NPs@NH_2-VMSF/ITO electrochemical immunosensor.

3 Results and discussion

3.1 Preparation of a Pt NPs@NH_2-VMSF/ITO-based immunosensor and its sensing mechanism for CEA

Scheme 1 reveals the fabrication process of the ITO electrode decorated with NH_2-VMSF, containing Pt nanostructures inside

10.3389/fchem.2023.1271556

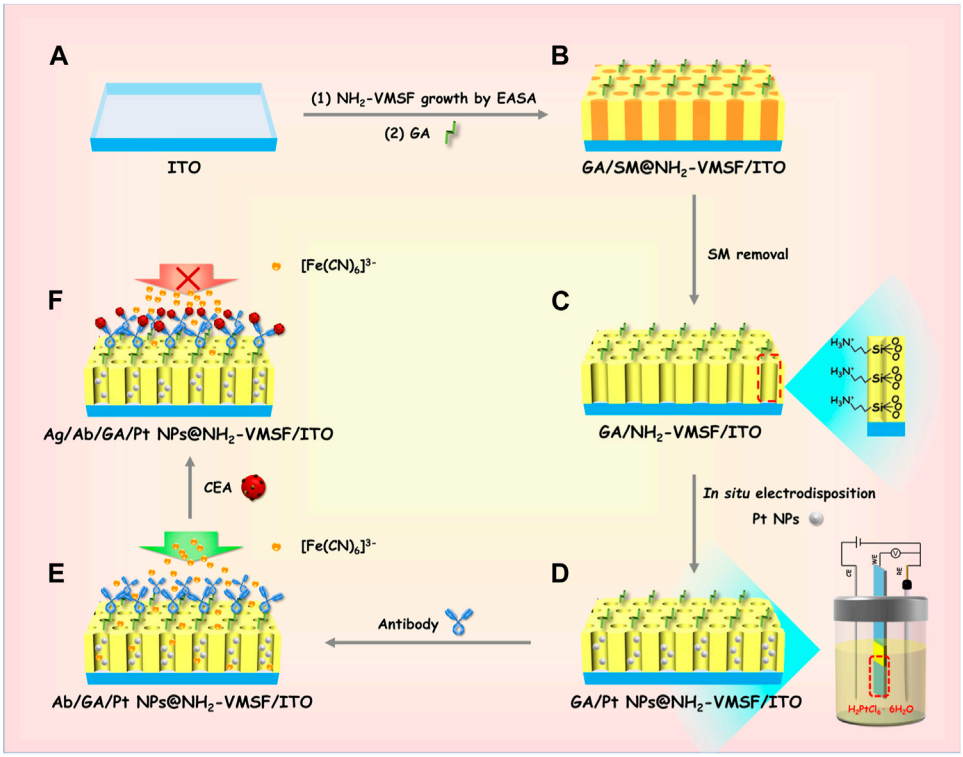

SCHEME 1
Schematic illustration of the preparation of the Ab/GA/Pt NPs@NH_2-VMSF/ITO electrode **(A–E)** and its sensing mechanism for the CEA **(A–F)**.

the inner nanochannels, while simultaneously modifying the anti-CEA antibody on the outmost surface using a convenient and controllable electrochemical method. The resulting electrode is termed as Ab/GA/Pt NPs@NH_2-VMSF/ITO, combining the electrocatalyst effect of Pt NPs and the specific recognition capacity of the anti-CEA antibody. The growth of NH_2-VMSF on the ITO electrode surface is accomplished by the EASA approach. Due to the presence of amine groups on both the inner silica walls and external surface, NH_2-VMSF-encased surfactant micelles inside the nanochannels are used to functionalize with a linker agent (glutaraldehyde, GA) (denoted as GA/SM@NH_2-VMSF/ITO, as shown in Scheme 1B), which can guarantee further modification of the anti-CEA antibody on the external surface of NH_2-VMSF. After exclusion of SMs, NH_2-VMSF possesses opened nanochannels and protonated amino groups on the silica walls, designated as GA/NH_2-VMSF/ITO (Scheme 1C), which renders the active sites for electrosynthesis of Pt NPs *in situ* to obtain GA/Pt NPs@NH_2-VMSF/ITO (Scheme 1D). Finally, the anti-CEA antibody is anchored to the external surface of NH_2-VMSF through GA, achieving the Ab/GA/Pt NPs@NH_2-VMSF/ITO sensor (Scheme 1E). The target CEA can be specially recognized on the Ab/GA/Pt NPs@NH_2-VMSF/ITO sensing interface, resulting in the hampered mass transport of the $[Fe(CN)_6]^{3-}$ probe in the bulk solution to the underlying ITO electrode surface through the silica nanochannels of NH_2-VMSF (Scheme 1F). Therefore, the decreased electrochemical current signal of $[Fe(CN)_6]^{3-}$ is associated with the CEA concentration, leading to the quantitative analytical method of detection of the CEA.

3.2 Characterization of NH_2-VMSF/ITO and Pt NPs@NH_2-VMSF/ITO electrodes

Figure 1 depicts the transmission electron microscopy and electrochemical characterization of NH_2-VMSF. A top-view TEM image of NH_2-VMSF displays a crack-free structure with numerous uniform pores of nanometer-sized diameter (ca. 2–3 nm) (Figure 1A). As shown in Figure 1B, the nanochannel of the NH_2-VMSF is homogeneous and its length is 79 nm. Figure 1C shows the CV curves of ITO, SM@NH_2-VMSF/ITO, and NH_2-VMSF/ITO electrodes in 0.05 M KHP containing 0.5 mM $K_3[Fe(CN)_6]$. The ITO electrode exhibits obvious redox peaks originating from the redox reaction of $[Fe(CN)_6]^{3-}$. However, the CV curve measured by the SM@NH_2-VMSF/ITO electrode shows no obvious redox peak, which is attributed to the hydrophobic environment consisting of CTAB SM and leads to the obstructed transport of hydrophilic $[Fe(CN)_6]^{3-}$ within nanochannels. The NH_2-VMSF/ITO electrode without SM inside the nanochannels not only has an open channel for free diffusion of $[Fe(CN)_6]^{3-}$ but also displays electrostatic attraction for negatively charged $[Fe(CN)_6]^{3-}$, eventually giving rise to amplified redox signals compared to those at the ITO. These results indicate that NH_2-VMSF on the ITO electrode is intact without cracks, and the

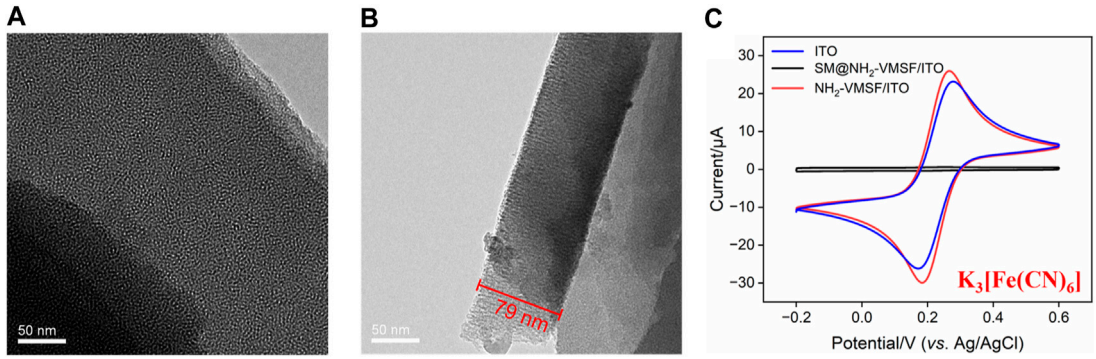

FIGURE 1
(A) Top-view TEM image of NH_2-VMSF. **(B)** Cross-sectional TEM image of NH_2-VMSF. **(C)** CV curves of the ITO, SM@NH_2-VMSF/ITO, and NH_2-VMSF/ITO electrodes in 0.05 M KHP containing 0.5 mM $K_3[Fe(CN)_6]$.

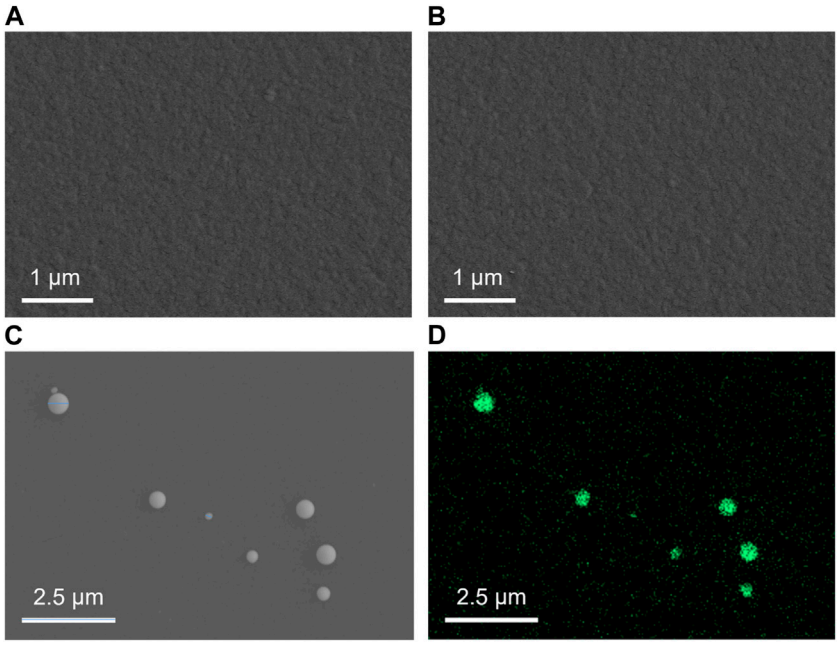

FIGURE 2
Top-view SEM images of NH_2-VMSF/ITO **(A)** and Pt NPs@NH_2-VMSF/ITO before **(B)** and after **(C)** the dissolution of NH_2-VMSF. **(D)** EDS elemental mapping of Pt NPs at the Pt NPs@NH_2-VMSF/ITO electrode after the dissolution of NH_2-VMSF.

electrochemical response of $[Fe(CN)_6]^{3-}$ at the NH_2-VMSF/ITO electrode can be enlarged, showing the significant potential of NH_2-VMSF/ITO for the design of gated-controlled electrochemical sensors.

Top-view SEM images in Figures 2A, B show the surface of the NH_2-VMSF/ITO electrode before and after the electrodeposition of Pt NPs. Both surfaces appear relatively smooth without obvious differences between NH_2-VMSF/ITO and Pt NPs@NH_2-VMSF/ITO, indicating that Pt NPs are confined inside the nanochannels. Figures 2C, D display the top-view SEM image and EDS elemental mapping of Pt NPs after dissolution of NH_2-VMSF by 0.1 M NaOH (50 μL). As seen, Pt NPs distributed on the surface of the electrode have sizes ranging from 160 to 260 nm, which is probably due to the aggregation of Pt NPs after losing the protection of NH_2-VMSF and also confirms the successful electrodeposition of Pt NPs within the nanochannels of NH_2-VMSF.

To further verify the successful electrodeposition of Pt NPs into the nanochannels of NH_2-VMSF, XPS analysis was conducted, as shown in Figure 3. As demonstrated, the presence of N and Pt in XPS data is derived from amino groups of NH_2-VMSF and electrodeposited Pt NPs, respectively. In addition, C, O, and Si elements are from the NH_2-VMSF structure. All the aforementioned results confirm the successful preparation of the Pt NPs@NH_2-VMSF/ITO electrode.

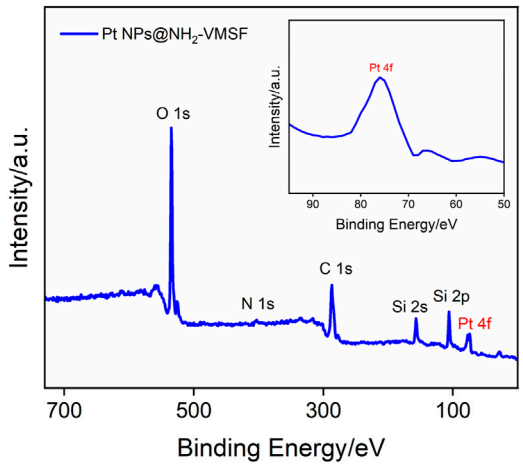

FIGURE 3
XPS survey spectra of Pt NPs@NH_2-VMSF/ITO.

3.3 Characterization of the Pt NPs@NH_2-VMSF/ITO-based electrochemical immunosensor

CV and EIS were used as electrochemical methods to investigate the interfacial state changes during the construction of the Ab/GA/Pt NPs@NH_2-VMSF/ITO sensor. Figure 4 displays the CV (A) and EIS (B) curves of NH_2-VMSF/ITO, GA/NH_2-VMSF/ITO, Pt NPs@NH_2-VMSF/ITO, GA/Pt NPs@NH_2-VMSF/ITO, Ab/GA/Pt NPs@NH_2-VMSF/ITO, and Ag/Ab/GA/Pt NPs@NH_2-VMSF/ITO electrodes in 50 mM KHP containing 0.5 mM $[Fe(CN)_6]^{3-}$. The cross-linking of GA with amino groups at the entrance of the silica nanochannels causes a decrease in redox peak current values of $[Fe(CN)_6]^{3-}$ at the GA/NH_2-VMSF/ITO and GA/Pt NPs@NH_2-VMSF/ITO, in comparison with those obtained at the NH_2-VMSF/ITO and Pt NPs@NH_2-VMSF/ITO (Figure 4A). After the successful electrodeposition of Pt NPs into the nanochannels of NH_2-VMSF, the magnitude of redox peak currents significantly increased due to the signal amplification capacity of Pt NPs. The redox peak currents further decrease after covalently attaching Ab to the GA/Pt NPs@NH_2-VMSF/ITO surface, which is attributed to the insulating property of proteins hindering the mass transfer of electrons on the electrode surface. Upon immobilization of CEA, the redox current values remarkably decrease, confirming the successful formation of the antibody–antigen immunocomplex at the sensing interface. EIS plots shown in Figure 4B consist of a semicircle part in the high-frequency region and a linear part in the low-frequency region, which are associated with the electron transfer and diffusion processes, respectively. Electron transfer resistance (R_{ct}) can be extracted from the magnitude of the semicircle diameter, showing the electron transfer variation between different electrodes. EIS measurements in Figure 4B reveal R_{ct} of the same electrodes shown in Figure 4A. Similar variation is observed, and GA/Pt NPs@NH_2-VMSF/ITO exhibits lower R_{ct} compared to GA/NH_2-VMSF/ITO, indicating that Pt NPs, as a kind of excellent electronic conductivity material, improve electron transfer ability on the electrode interface. Moreover, R_{ct} significantly increases after immobilization of the anti-CEA antibody and target CEA, demonstrating that the formed antibody–antigen immunocomplex indeed obstructs the diffusion of electrons and further proving the feasible detection capacity of the developed Ab/GA/Pt NPs@NH_2-VMSF/ITO.

3.4 Optimization of experimental conditions

There are several factors that affect the analytical performance of the Ab/GA/Pt NPs@NH_2-VMSF/ITO sensor, including the electrodeposition time of Pt NPs and the incubation time of the anti-CEA antibody or CEA. First, we studied the performance of the developed sensor with various electrodeposition times of Pt NPs ranging from 1 s to 10 s (Figure 5A). When the electrodeposition time increases from 1 s to 2 s, the obtained DPV signal for CEA increases due to the increased amount of Pt NPs and reaches its

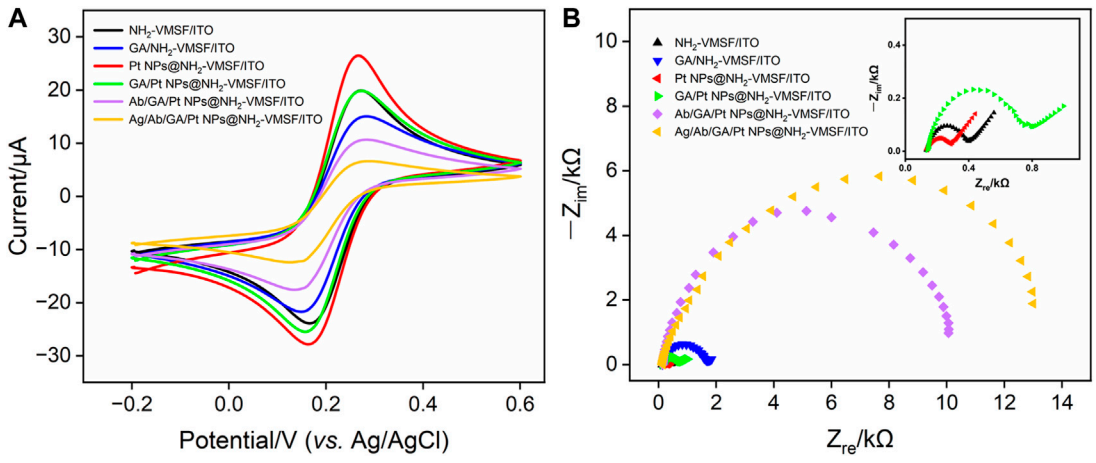

FIGURE 4
(A) CV curves of different electrodes in 50 mM KHP containing 0.5 mM $K_3[Fe(CN)_6]$ and **(B)** EIS curves of different electrodes in 0.1 M KCl containing 2.5 mM $[Fe(CN)_6]^{3-}/[Fe(CN)_6]^{4-}$.

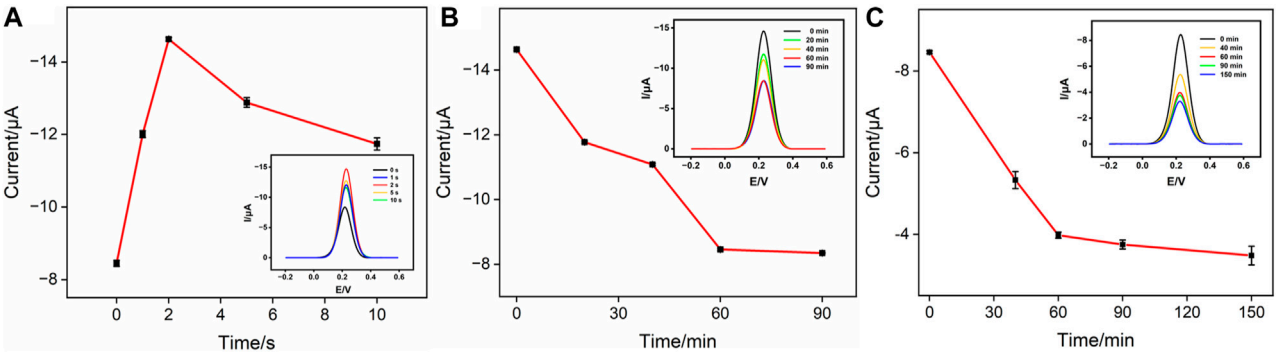

FIGURE 5
(A) Cathodic peak currents measured at the GA/Pt NPs@NH_2-VMSF/ITO in 50 mM KHP containing 0.5 mM $K_3[Fe(CN)_6]$ at different deposition times of Pt NPs. The inset shows its corresponding DPV curves. **(B)** Cathodic peak currents measured at the Ab/GA/Pt NPs@NH_2-VMSF/ITO in 50 mM KHP containing 0.5 mM $K_3[Fe(CN)_6]$ at different incubation times for the anti-CEA antibody. The inset shows its corresponding DPV curves. **(C)** Cathodic peak currents measured at the Ag/Ab/GA/Pt NPs@NH_2-VMSF/ITO in 50 mM KHP containing 0.5 mM $K_3[Fe(CN)_6]$ at different incubation times for the CEA. The inset shows its corresponding DPV curves.

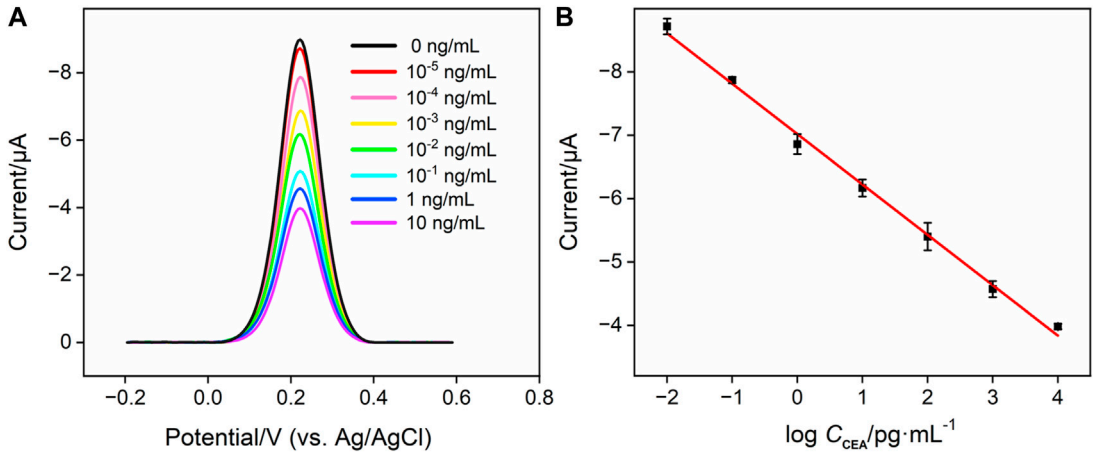

FIGURE 6
(A) DPV responses of the Ag/Ab/GA/Pt NPs@NH_2-VMSF electrode to various concentrations of CEA in 0.01 M PBS (pH 7.4). **(B)** Corresponding calibration curves. Error bars refer to the standard deviations of three measurements.

maximum when the deposition time is set to 2 s. When the electrodeposition time further increases from 2 s to 10 s, the signal gradually decreases. This decrease can be attributed to the reduced effective space of NH_2-VMSF's nanochannels for accessible transport of the $[Fe(CN)_6]^{3-}$ probe in the bulk solution. Subsequently, we investigated the incubation time of the anti-CEA antibody. As displayed in Figure 5B, it could be found that the peak current intensity decreases as the incubation time increases up to 60 min. This is because the amount of anti-CEA immobilized on the electrode is approaching saturation. Similarly, the effect of incubation time for the CEA on the electrochemical response is shown in Figure 5C. It is evident that as the incubation time increases, the peak current signal gradually decreases. After incubation for more than 60 min, the signal changes become minimal, indicating that the immunocomplex formed between the CEA and anti-CEA antibody has reached saturation. Therefore, 60 min is determined to be the optimal incubation time.

3.5 Quantitative determination of CEA using the fabricated Ab/GA/Pt NPs@NH_2-VMSF/ITO immunosensor

To evaluate the analytical performance of the Ab/GA/Pt NPs@NH_2-VMSF/ITO sensor, we tested it in detecting the CEA with various concentrations under optimized conditions using the DPV technique. As shown in Figure 6A, the cathodic peak current decreased progressively with the increase in the concentration of the CEA due to the continuous formation of the antibody–antigen complex at the sensing interface. A good linear relationship is displayed between the DPV signal (I_{DPV}) and the logarithm of the CEA concentration (C_{CEA}) in the range of 0.01 pg/mL to 10 ng/mL (Figure 6B), yielding a linear regression equation of I_{DPV} (μA) = 0.796 logC_{CEA}-7.02 (R^2 = 0.996). Furthermore, the limit of detection (LOD) calculated is 0.3 fg/mL at the signal-to-noise ratio of 3 (S/N = 3). We compare the related analytical parameters and construction

TABLE 1 Comparison of the analytical performances of different methods for the determination of the CEA.

Sensing platform	Method	Detection range (ng/mL)	LOD (pg/mL)	Step	Construction time (h)	Reference
BSA/Ab/Pd@Pt/MoS_2-Gr/GCE	EC	0.00001–100	0.005	13	39	Lin et al. (2021)
CuO NPs/Ag/BSA/Ab/MB	Colorimetry	0.05–100	26	8	5	Li et al. (2017)
PdCu-Ab_2/Ag/Ab_1/BSA/AuNPs/GCE	EC	0.0001–10	0.08	7	16	Jiao et al. (2017)
GO-PEI-Ru-AuNPs-Ab_2/Ag/Ab_1/AuNFs/pL-Cys/GCE	ECL	0.0001–80	0.045	12	37	Yuan et al. (2018)
CEA aptamer/ZnS-CdS/MoS_2/GCE	ECL	0.05–20	30	8	60	Wang et al. (2016)
Ab/AuNPs@nafion/FC@CHIT/GCE	EC	0.03–100	10	9	8	Shi and Ma (2011)
Ab/GA/Pt NPs@NH_2-VMSF/ITO	EC	0.0001–10	0.0003	7	5	This work

BSA, bovine serum albumin; Ab, the antibody of the CEA; MoS_2, molybdenum disulfide; Gr, graphene; GCE, glassy carbon electrode; CuO NPs, copper oxide nanoparticle; Ag, carcinoembryonic antigen; MB, magnetic bead; PdCu, porous PdCu nanoparticles; AuNPs, gold nanoparticles; GO, graphene oxide; PEI, polyethylenimine; Ru, the luminophor tris (4,40-dicarboxylicacid-2, 20-bipyridyl) ruthenium (II) dichloride ($Ru(dcbpy)_3^{2+}$); AuNFs, flower-like gold nanoparticles; pL-Cys, polyamino acid L-cysteine; ZnS–CdS, ZnS–CdS nanoparticle; FC: $K_3[Fe(CN)_6]$; CHIT, chitosan.

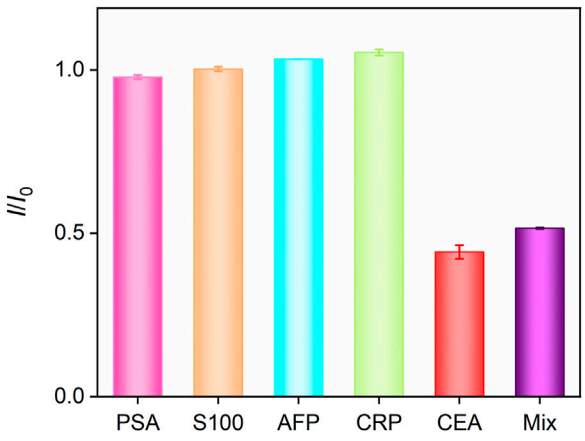

FIGURE 7
DPV current ratio obtained from Ab/GA/Pt NPs@NH_2-VMSF/ITO in the absence (I_0) or presence (I) of different species with the same concentration (10 ng/mL). Error bars refer to the standard deviations of three measurements.

strategy of the Ab/GA/Pt NPs@NH_2-VMSF/ITO sensor with the other reported sensors. As shown in Table 1, our fabricated Ab/GA/Pt NPs@NH_2-VMSF/ITO strategy has a low LOD and simple preparation steps. Moreover, the developed sensor not only achieves dual signal amplification through the electrocatalysis ability of Pt NPs and the electrostatic enrichment effect of VMSF at the electrode interface but also has the advantage of a shorter construction time.

3.6 Selectivity of the fabricated Ab/GA/Pt NPs@NH_2-VMSF/ITO immunosensor

The selectivity of the fabricated Ab/GA/Pt NPs@NH_2-VMSF/ITO sensor were studied by multiple potential interfering substances, including the PSA, S100 calcium-binding protein β, AFP, and CRP. As shown in Figure 7, the Ab/GA/Pt NPs@NH_2-VMSF/ITO immunosensor demonstrates excellent signal response to the CEA and a mixture of the aforementioned substances containing the CEA while showing almost no response to other interfering substances. This indicates that our sensing platform has high selectivity to the CEA, resulting from the specific binding of the anti-CEA antibody and CEA complex.

3.7 Detection of CEA in real samples

To validate the reliability and accuracy of the developed Ab/GA/Pt NPs@NH_2-VMSF/ITO sensor, we conducted real sample testing by detecting the CEA amount in fetal bovine serum using the standard addition method. After diluting the fetal bovine serum by a factor of 50 using 0.01 M PBS (pH 7.4), we added 0.1 pg/mL, 10 pg/mL, and 1000 pg/mL of CEA and measured the electrochemical signals by DPV. The added known and tested concentrations of the CEA are designated as "C_{added}" and "C_{found}". In addition, the recovery is defined as the concentration ratio ((C_{added}/C_{found})×100%), which is used to evaluate the detection performance of the fabricated Ab/GA/Pt NPs@NH_2-VMSF/ITO in real samples. Generally, recovery ranging from 90.0% to 110% is considered for high accuracy. The relative standard deviation (RSD) value represents the deviation of three measurements disseminated around the average value, which is expressed as the ratio of the standard deviation to the average value. The lower the RSD, the closer the measured values are to the average value, indicating good precision. As shown in Table 2, the recoveries of the CEA obtained in the aforementioned fetal bovine serum samples range from 104.5% to 107.4% with low RSD values (<5.7%). These results demonstrate the promising potential of the proposed Ab/GA/Pt NPs@NH_2-VMSF/ITO sensor for sensitive detection of the CEA in clinical applications.

TABLE 2 Recoveries of the CEA in the fetal bovine serum sample (n = 3).

Sample	C_{Added} (pg·mL^{-1})	C_{Found} (pg·mL^{-1})	Recovery (%)	RSD (%)
Serum	0.1000	0.1060	106.0	3.1
	10.00	10.45	104.5	5.7
	1000	1074	107.4	2.8

4 Conclusion

In summary, Pt NPs confined in the silica nanochannels of NH_2-VMSF without any protecting ligands have been successfully synthesized on the ITO electrode surface using a simple electrochemical method. The CEA antibody covalently modified on the external surface of NH_2-VMSF endows the sensor with good specificity for CEA detection. With the help of the $[Fe(CN)_6]^{3-}$ probe in the bulk solution, the high affinity between the CEA antibody and CEA on the sensing interface forms the steric hindrance effect for the accessibility of $[Fe(CN)_6]^{3-}$ to the underlying ITO surface, resulting in an attenuated electrochemical signal and allowing the detection of the CEA with a wide linear range of 0.01 pg/mL~10 ng/mL and a pretty low limit of detection of 0.30 fg/mL. Combining the signal amplification ability of Pt NPs and the anti-biofouling property of NH_2-VMSF, the presented sensing strategy can be directly applied in detecting the CEA in human serum samples, which is helpful for the analysis of tumor-related biomarkers in clinical diagnosis.

Data availability statement

The original contributions presented in the study are included in the article/Supplementary material; further inquiries can be directed to the corresponding authors.

Author contributions

QG: data curation, formal analysis, methodology, and writing–original draft. XF: formal analysis, methodology, validation, and writing–original draft. FY: project administration, supervision, and writing–review and editing. YW: conceptualization, supervision, and writing–review and editing.

Funding

The authors declare that financial support was received for the research, authorship, and/or publication of this article. This study was funded by the Shanxi Province 136 Revitalization Medical Project Construction Funds, the Zhejiang Provincial Natural Science Foundation of China (LY21B050003), and the Fundamental Research Funds of Zhejiang Sci-Tech University (22062310-Y).

Conflict of interest

The authors declare that the research was conducted in the absence of any commercial or financial relationships that could be construed as a potential conflict of interest.

Publisher's note

All claims expressed in this article are solely those of the authors and do not necessarily represent those of their affiliated organizations, or those of the publisher, the editors, and the reviewers. Any product that may be evaluated in this article, or claim that may be made by its manufacturer, is not guaranteed or endorsed by the publisher.

References

Chen, D., Luo, X., and Xi, F. (2023). Probe-integrated electrochemical immunosensor based on electrostatic nanocage array for reagentless and sensitive detection of tumor biomarker. *Front. Chem.* 11, 1121450. doi:10.3389/fchem.2023.1121450

Cui, Y., Duan, W., Jin, Y., Wo, F., Xi, F., and Wu, J. (2021). Graphene quantum dot-decorated luminescent porous silicon dressing for theranostics of diabetic wounds. *Acta Biomater.* 131, 544–554. doi:10.1016/j.actbio.2021.07.018

Cui, Y., Duan, W., Jin, Y., Wo, F., Xi, F., and Wu, J. (2020). Ratiometric fluorescent nanohybrid for noninvasive and visual monitoring of sweat glucose. *ACS Sens.* 5, 2096–2105. doi:10.1021/acssensors.0c00718

Deng, X., Lin, X., Zhou, H., Liu, J., and Tang, H. (2023). Equipment of vertically-ordered mesoporous silica film on electrochemically pretreated three-dimensional graphene electrodes for sensitive detection of methidazine in urine. *Nanomaterials* 13, 239. doi:10.3390/nano13020239

Ding, J., Li, X., Zhou, L., Yang, R., Yan, F., and Su, B. (2020). Electrodeposition of nickel nanostructures using silica nanochannels as confinement for low-fouling enzyme-free glucose detection. *J. Mat. Chem. B* 8, 3616–3622. doi:10.1039/c9tb02472g

Ding, L., Li, W., Sun, Q., He, Y., and Su, B. (2014a). Gold nanoparticles confined in vertically aligned silica nanochannels and their electrocatalytic activity toward ascorbic acid. *Chem.-Eur. J.* 20, 12777–12780. doi:10.1002/chem.201403426

Ding, L., Li, W., Wang, Q., Sun, Q., He, Y., and Su, B. (2014b). Vertically oriented silica mesochannels as the template for electrodeposition of polyaniline nanostructures and their electrocatalytic and electroanalytical applications. *Chem.-Eur. J.* 20, 1829–1833. doi:10.1002/chem.201303807

Ding, L., and Su, B. (2015). A non-enzymatic hydrogen peroxide sensor based on platinum nanoparticle-polyaniline nanocomposites hosted in mesoporous silica film. *J. Electroanal. Chem.* 736, 83–87. doi:10.1016/j.jelechem.2014.11.001

Edgington, T. S., Plow, E. F., Chavkin, C. I., Deheer, D. T., and Nakamura, R. M. (1976). The influence of CEA-S from different tumors and of CEA as 125I ligands on the specificity of the CEA-S radioimmunoassay. *B. Cancer* 63, 673–688.

Etienne, M., Goux, A., Sibottier, E., and Walcarius, A. (2009). Oriented mesoporous organosilica films on electrode: a new class of nanomaterials for sensing. *J. Nanosci. Nanotechno.* 9, 2398–2406. doi:10.1166/jnn.2009.se39

Gong, J., Tang, H., Wang, M., Lin, X., Wang, K., and Liu, J. (2022a). Novel three-dimensional graphene nanomesh prepared by facile electro-etching for improved

electroanalytical performance for small biomolecules. *Mat. Des.* 215, 110506. doi:10.1016/j.matdes.2022.110506

Gong, J., Zhang, T., Luo, T., Luo, X., Yan, F., Tang, W., et al. (2022b). Bipolar silica nanochannel array confined electrochemiluminescence for ultrasensitive detection of SARS-CoV-2 antibody. *Biosens. Bioelectron.* 215, 114563. doi:10.1016/j.bios.2022.114563

Huang, J., Zhang, T., Zheng, Y., and Liu, J. (2023a). Dual-mode sensing platform for cancer antigen 15-3 determination based on a silica nanochannel array using electrochemiluminescence and electrochemistry. *Biosensors* 13, 317. doi:10.3390/bios13030317

Huang, L., Su, R., and Xi, F. (2023b). Sensitive detection of noradrenaline in human whole blood based on Au nanoparticles embedded vertically-ordered silica nanochannels modified pre-activated glassy carbon electrodes. *Front. Chem.* 11, 1126213. doi:10.3389/fchem.2023.1126213

Huang, Y., Ding, Z., Li, Y., Xi, F., and Liu, J. (2023c). Magnetic nanozyme based on loading nitrogen-doped carbon dots on mesoporous Fe_3O_4 nanoparticles for the colorimetric detection of glucose. *Molecules* 28, 4573. doi:10.3390/molecules28124573

Huang, Z., Zhai, X. M., Wang, H., Deng, Q. T., Li, K., Liu, B. S., et al. (2018). Simultaneous quantitation of carbohydrate antigen 125 and carcinoembryonic antigen in human serum via time-resolved fluoroimmunoassay. *Clin. Chim. Acta.* 483, 222–226. doi:10.1016/j.cca.2018.05.003

Jiao, L., Zhang, L., Du, W., Liu, S., Wei, Q., and Li, H. (2017). Robust enzyme-free electrochemical immunoassay of CEA enhanced by porous PdCu nanoparticles. *Electrochim. Acta.* 252, 374–380. doi:10.1016/j.electacta.2017.08.188

Li, B., Lai, G., Zhang, H., Hu, S., and Yu, A. (2017). Copper chromogenic reaction based colorimetric immunoassay for rapid and sensitive detection of a tumor biomarker. *Anal. Chim. Acta.* 963, 106–111. doi:10.1016/j.aca.2017.01.030

Li, X., Zhou, L., Ding, J., Sun, L., and Su, B. (2020). Platinized silica nanoporous membrane electrodes for low-fouling hydrogen peroxide detection. *ChemElectroChem* 7, 2081–2086. doi:10.1002/celc.202000321

Liang, R., Jiang, J., Zheng, Y., Sailjoi, A., Chen, J., Liu, J., et al. (2021). Vertically oriented mesoporous silica film modified fluorine-doped tin oxide electrode for enhanced electrochemiluminescence detection of lidocaine in serum. *RSC Adv.* 11, 34669–34675. doi:10.1039/d1ra06375h

Lin, J., Li, K., Wang, M., Chen, X., Liu, J., and Tang, H. (2020). Reagentless and sensitive determination of carcinoembryonic antigen based on a stable Prussian blue modified electrode. *RSC Adv.* 10, 38316–38322. doi:10.1039/d0ra06751b

Lin, Y., Xiong, C., Shi, J., Zhang, J., and Wang, X. (2021). Electrochemical immunosensor based on Pd@Pt/MoS_2-Gr for the sensitive detection of CEA. *J. Solid State Electrochem.* 25, 2075–2085. doi:10.1007/s10008-021-04978-y

Liu, X., Chen, Z., Wang, T., Jiang, X., Qu, X., Duan, W., et al. (2022). Tissue imprinting on 2D nanoflakes-capped silicon nanowires for lipidomic mass spectrometry imaging and cancer diagnosis. *ACS Nano* 16, 6916–6928. doi:10.1021/acsnano.2c02616

Luo, X., Zhang, T., Tang, H., and Liu, J. (2022). Novel electrochemical and electrochemiluminescence dual-modality sensing platform for sensitive determination of antimicrobial peptides based on probe encapsulated liposome and nanochannel array electrode. *Front. Nutr.* 9, 962736. doi:10.3389/fnut.2022.962736

Lv, N., Qiu, X., Han, Q., Xi, F., Wang, Y., and Chen, J. (2022). Anti-biofouling electrochemical sensor based on the binary nanocomposite of silica nanochannel array and graphene for doxorubicin detection in human serum and urine samples. *Molecules* 27, 8640. doi:10.3390/molecules27248640

Ma, K., Yang, L., Liu, J., and Liu, J. (2022a). Electrochemical sensor nanoarchitectonics for sensitive detection of uric acid in human whole blood based on screen-printed carbon electrode equipped with vertically-ordered mesoporous silica-nanochannel film. *Nanomaterials* 12, 1157. doi:10.3390/nano12071157

Ma, K., Zheng, Y., An, L., and Liu, J. (2022b). Ultrasensitive immunosensor for prostate-specific antigen based on enhanced electrochemiluminescence by vertically ordered mesoporous silica-nanochannel film. *Front. Chem.* 10, 851178. doi:10.3389/fchem.2022.851178

Ma, N., Luo, X., Wu, W., and Liu, J. (2022c). Fabrication of a disposable electrochemical immunosensor based on nanochannel array modified electrodes and gated electrochemical signals for sensitive determination of C-reactive protein. *Nanomaterials* 12, 3981. doi:10.3390/nano12223981

Mao, Y., Zhao, C., Ge, S., Luo, T., Chen, J., Liu, J., et al. (2019). Gram-scale synthesis of nitrogen doped graphene quantum dots for sensitive detection of mercury ions and l-cysteine. *RSC Adv.* 9, 32977–32983. doi:10.1039/c9ra06113d

Qiu, G., Han, Y., Zhu, X., Gong, J., Luo, T., Zhao, C., et al. (2021). Sensitive detection of sulfide ion based on fluorescent ionic liquid-graphene quantum dots nanocomposite. *Front. Chem.* 9, 658045. doi:10.3389/fchem.2021.658045

Shi, W., and Ma, Z. (2011). A novel label-free amperometric immunosensor for carcinoembryonic antigen based on redox membrane. *Biosens. Bioelectron.* 26, 3068–3071. doi:10.1016/j.bios.2010.11.048

Song, G., Zhou, H., Gu, J., Liu, Q., Zhang, W., Su, H., et al. (2017). Tumor marker detection using surface enhanced Raman spectroscopy on 3D Au butterfly wings. *J. Mat. Chem. B* 5, 1594–1600. doi:10.1039/c6tb03026b

Su, R., Tang, H., and Xi, F. (2022). Sensitive electrochemical detection of p-nitrophenol by pre-activated glassy carbon electrode integrated with silica nanochannel array film. *Front. Chem.* 10, 954748. doi:10.3389/fchem.2022.954748

Tang, H., Chen, J., Nie, L., Kuang, Y., and Yao, S. (2007). A label-free electrochemical immunoassay for carcinoembryonic antigen (CEA) based on gold nanoparticles (AuNPs) and nonconductive polymer film. *Biosens. Bioelectron.* 22, 1061–1067. doi:10.1016/j.bios.2006.04.027

Walcarius, A. (2021). Electroinduced surfactant self-assembly driven to vertical growth of oriented mesoporous films. *Acc. Chem. Res.* 54, 3563–3575. doi:10.1021/acs.accounts.1c00233

Wang, K., Yang, L., Huang, H., Lv, N., Liu, J., and Liu, Y. (2022). Nanochannel array on electrochemically polarized screen printed carbon electrode for rapid and sensitive electrochemical determination of clozapine in human whole blood. *Molecules* 27, 2739. doi:10.3390/molecules27092739

Wang, Y. L., Cao, J. T., Chen, Y. H., and Liu, Y. M. (2016). A label-free electrochemiluminescence aptasensor for carcinoembryonic antigen detection based on electrodeposited ZnS–CdS on MoS_2 decorated electrode. *Anal. Methods* 8, 5242–5247. doi:10.1039/c6ay01114d

Wei, X., Luo, X., Xu, S., Xi, F., and Zhao, T. (2022). A flexible electrochemiluminescence sensor equipped with vertically ordered mesoporous silica nanochannel film for sensitive detection of clindamycin. *Front. Chem.* 10, 872582. doi:10.3389/fchem.2022.872582

White, R. J., Luque, R., Budarin, V. L., Clark, J. H., and Macquarrie, D. J. (2009). Supported metal nanoparticles on porous materials. Methods and applications. *Chem. Soc. Rev.* 38, 481–494. doi:10.1039/b802654h

Xi, F., Zhao, J., Shen, C., He, J., Chen, J., Yan, Y., et al. (2019). Amphiphilic graphene quantum dots as a new class of surfactants. *Carbon* 153, 127–135. doi:10.1016/j.carbon.2019.07.014

Xu, S., Zhang, S., Li, Y., and Liu, J. (2023). Facile synthesis of iron and nitrogen Co-doped carbon dot nanozyme as highly efficient peroxidase mimics for visualized detection of metabolites. *Molecules* 28, 6064. doi:10.3390/molecules28166064

Yan, Z., Zhang, S., Liu, J., and Xing, J. (2023). Homogeneous electrochemical aptamer sensor based on two-dimensional nanocomposite probe and nanochannel modified electrode for sensitive detection of carcinoembryonic antigen. *Molecules* 28, 5186. doi:10.3390/molecules28135186

Yuan, Y., Zhang, L., Wang, H., Chai, Y., and Yuan, R. (2018). Self-enhanced PEI-Ru(II) complex with polyamino acid as booster to construct ultrasensitive electrochemiluminescence immunosensor for carcinoembryonic antigen detection. *Anal. Chim. Acta.* 1001, 112–118. doi:10.1016/j.aca.2017.11.035

Zeng, Z., Cohen, A. M., and Urmacher, C. (1993). Usefulness of carcinoembryonic antigen monitoring despite normal preoperative values in node-positive colon cancer patients. *Dis. Colon. Rectum* 36, 1063–1068. doi:10.1007/bf02047301

Zhang, A., Huang, C., Shi, H., Guo, W., Zhang, X., Xiang, H., et al. (2017). Electrochemiluminescence immunosensor for sensitive determination of tumor biomarker CEA based on multifunctionalized Flower-like Au@BSA nanoparticles. *Sens. Actuators. B Chem.* 238, 24–31. doi:10.1016/j.snb.2016.07.009

Zhang, C., Zhou, X., Yan, F., and Lin, J. (2023a). N-doped graphene quantum dots confined within silica nanochannels for enhanced electrochemical detection of doxorubicin. *Molecules* 28, 6443. doi:10.3390/molecules28186443

Zhang, J., Yang, L., Pei, J., Tian, Y., and Liu, J. (2022). A reagentless electrochemical immunosensor for sensitive detection of carcinoembryonic antigen based on the interface with redox probe-modified electron transfer wires and effectively immobilized antibody. *Front. Chem.* 10, 939736. doi:10.3389/fchem.2022.939736

Zhang, T., Xu, S., Lin, X., Liu, J., and Wang, K. (2023b). Label-free electrochemical aptasensor based on the vertically-aligned mesoporous silica films for determination of aflatoxin B1. *Biosensors* 13, 661. doi:10.3390/bios13060661

Zhao, X., Zhao, H., Yan, L., Li, N., Shi, J., and Jiang, C. (2020). Recent developments in detection using noble metal nanoparticles. *Crit. Rev. Anal. Chem.* 50, 97–110. doi:10.1080/10408347.2019.1576496

Zheng, W., Su, R., Lin, X., and Liu, J. (2022). Nanochannel array modified three-dimensional graphene electrode for sensitive electrochemical detection of 2,4,6-trichlorophenol and prochloraz. *Front. Chem.* 10, 954802. doi:10.3389/fchem.2022.954802

Zheng, Y., Lin, J., Xie, L., Tang, H., Wang, K., and Liu, J. (2021). One-step preparation of nitrogen-doped graphene quantum dots with anodic electrochemiluminescence for sensitive detection of hydrogen peroxide and glucose. *Front. Chem.* 9, 688358. doi:10.3389/fchem.2021.688358

Zhou, H., Ding, Y., Su, R., Lu, D., Tang, H., and Xi, F. (2022). Silica nanochannel array film supported by ß-cyclodextrin-functionalized graphene modified gold film electrode for sensitive and direct electroanalysis of acetaminophen. *Front. Chem.* 9, 812086. doi:10.3389/fchem.2021.812086

Zhou, X., Han, Q., Zhou, J., Liu, C., and Liu, J. (2023). Reagentless electrochemical detection of tumor biomarker based on stable confinement of electrochemical probe in bipolar silica nanochannel film. *Nanomaterials* 13, 1645. doi:10.3390/nano13101645

Zhu, D., Tan, Y., Zheng, L., Lao, J., Liu, J., Yu, J., et al. (2023). Microneedle-coupled epidermal sensors for in-situ-multiplexed ion detection in interstitial fluids. *ACS Appl. Mat. Interfaces* 15, 14146–14154. doi:10.1021/acsami.3c00573

Zhu, X., Xuan, L., Gong, J., Liu, J., Wang, X., Xi, F., et al. (2022). Three-dimensional macroscopic graphene supported vertically-ordered mesoporous silica-nanochannel film for direct and ultrasensitive detection of uric acid in serum. *Talanta* 238, 123027. doi:10.1016/j.talanta.2021.123027